



HAL
open science

Thermodynamics versus kinetics in a morphology transition of nanoparticles

H. Bulou, F. Scheurer, C. Goyhenex, V. Speisser, M. Romeo, B. Carriere, N. Moreau, V. Repain, C. Chacon, Y. Girard, et al.

► **To cite this version:**

H. Bulou, F. Scheurer, C. Goyhenex, V. Speisser, M. Romeo, et al.. Thermodynamics versus kinetics in a morphology transition of nanoparticles. *Physical Review B*, 2013, 87 (15), 10.1103/PhysRevB.87.155404 . hal-01987561

HAL Id: hal-01987561

<https://hal.science/hal-01987561>

Submitted on 21 Aug 2023

HAL is a multi-disciplinary open access archive for the deposit and dissemination of scientific research documents, whether they are published or not. The documents may come from teaching and research institutions in France or abroad, or from public or private research centers.

L'archive ouverte pluridisciplinaire **HAL**, est destinée au dépôt et à la diffusion de documents scientifiques de niveau recherche, publiés ou non, émanant des établissements d'enseignement et de recherche français ou étrangers, des laboratoires publics ou privés.

Thermodynamics versus kinetics in a morphology transition of nanoparticles

H. Bulou,^{1,*} F. Scheurer,¹ C. Goyhenex,¹ V. Speisser,¹ M. Romeo,¹ B. Carrière,¹ N. Moreau,² V. Repain,² C. Chacon,² Y. Girard,² J. Lagoute,² S. Rousset,² E. Otero,³ and P. Ohresser³

¹*Institut de Physique et Chimie des Matériaux de Strasbourg, Université de Strasbourg & CNRS, UMR 7504, 23 rue du Loess, F-67034 Strasbourg, France*

²*Laboratoire Matériaux et Phénomènes Quantiques, Université Diderot & CNRS, UMR 7162, Case Courrier 7021, F-75205 Paris, France*

³*Synchrotron-SOLEIL, L'Orme des merisiers Saint-Aubin, BP 48, F-91192 Gif-sur-Yvette cedex, France*

(Received 4 July 2011; revised manuscript received 4 December 2012; published 8 April 2013)

The morphology of cobalt, palladium, and platinum nanoclusters grown on a gold surface is analyzed from both thermodynamic and kinetic viewpoints. Although the thermodynamic equilibrium shape as a function of cluster size is similar for all three elements and shows a morphology transition from monolayer to bilayer, only Co clusters meet their stable state and undergo a transition. Atomistic simulations on a picosecond to nanosecond time scale evidence kinetic limitations for Pt and Pd, and allow us to understand the experimentally observed morphology for the different species. It is shown that stress relaxation, by strongly influencing the energy activation for atom hopping from first to second cluster layer and the magnitude of vibration of the atoms, is the determinant parameter for the existence or absence of the cluster morphology transition.

DOI: [10.1103/PhysRevB.87.155404](https://doi.org/10.1103/PhysRevB.87.155404)

PACS number(s): 68.35.Md, 68.43.Jk

I. INTRODUCTION

Since the pioneering work of Faraday on the color of ruby,¹ the relationship between morphology and particle properties has been evidenced in many domains, including catalysis,² magnetism,³ and optics.⁴ Nowadays, a major challenge is to shape the particle at a nanoscopic scale to reach specific properties resulting from the combination of reduced dimensionality and controlled morphology, such as the plasmon resonances⁵ and the morphologically controlled catalytic⁶ or magnetic behavior.⁷

Controlling the shape of particles at a nanoscopic scale is not a simple task because particle growth involves numerous atomic processes, such as surface and interlayer diffusion,^{8,9} exchange mechanism,¹⁰ and/or long range mass transport.^{11,12} The control of the particle shape needs then to regulate the energy distribution between the different phenomena and different parts of the system, as well as to exert an efficient control on the time scale of the processes. The main objective of this work is to unravel thermodynamic from kinetic effects during particle growth, with a focus on the role of elastic stress and chemical energy at the interface.^{13,14}

Thermodynamics rules the energy exchanges governing the evolution of a particle, whereas kinetics refers to the atomistic mechanisms at the origin of mass transport and its typical time scale. In a previous work, we studied the morphology of Co clusters supported on a gold surface from a purely thermodynamic point of view.^{15,16} We evidenced the coexistence of two types of Co clusters having either a monolayer or a bilayer height, depending on their size when deposited on a gold substrate. In the present paper, we extend this work to Pd and Pt clusters and we show that thermodynamic arguments alone cannot explain the experimentally observed morphologies for these two elements, in contrast to Co. We therefore revisit the morphology of Co, Pt, and Pd nanoclusters on Au(111) from a kinetic point of view by classical molecular dynamics on a picosecond to nanosecond time scale. Comparing the three systems allows us to understand the role of the different energy contributions, namely stress and chemical energy. We show

that the kinetics of the monolayer to bilayer transition is mainly determined by the stress inside the nanocluster. An analysis of crystal vibrations gives new insights on the mechanisms at work in the monolayer to bilayer transition.

II. EXPERIMENTAL AND CALCULATION DETAILS

Cluster morphologies were observed with scanning tunneling microscopy (STM), in an ultrahigh vacuum chamber with a base pressure of 5×10^{-11} mbar. All experiments were performed using Au(111) oriented single crystals, prepared by Ar⁺ ion sputtering and 1000 K annealing cycles. Co, Pd, and Pt were deposited from high purity rods in electron bombardment cells equipped with flux monitors. The flux monitors were calibrated with STM by repeated deposition of fractions of a monolayer up to one monolayer, corresponding to a fully covered substrate. Deposition rates are on the order of one monolayer (ML) in 20 minutes. During metal deposition, the substrate was held at room temperature.

The molecular dynamics process consists in integrating Newton's equations for all atoms of the system. The forces involved in the process were derived from the total energy, defined as the sum of the overall site energies. The site energies are based on effective potentials determined in the second-moment approximation of the tight binding theory¹⁷ (TBSMA) with the constraints (i) to reproduce for the mixed interactions the main features of the phase diagrams, and for pure interactions the cohesive energy, the lattice parameter, the bulk modulus and the elastic constants; (ii) to preserve the correct surface energy difference for each couple of pure metals.^{15,16,18,19}

The energy of an atom at site i is the sum of an attractive band energy $E_i^{(b)}$ and a repulsive pair interaction $E_i^{(r)}$:

$$E_i^{(b)} = \sqrt{\sum_{j \neq i}^{N_{\text{atom}}} \xi_{ij}^2 \exp \left[-2q_{ij} \left(\frac{r_{ij}}{r_{ij}^{(0)}} - 1 \right) \right]}, \quad (1)$$

$$E_i^{(r)} = \sum_{j \neq i}^{N_{\text{atom}}} A_{ij} \exp \left[- p_{ij} \left(\frac{r_{ij}}{r_{ij}^{(0)}} - 1 \right) \right]. \quad (2)$$

The parameters of the interactions are given in Table II (see Appendix). The time integration was performed by using a velocities Verlet integration algorithm.^{20,21} Molecular dynamics was also used as an optimization tool through a quenching procedure to minimize the potential energy.²² Additional velocity modifications and adaptive time steps to accelerate the quenching process were used during energy minimization.²³ In order to avoid local minima, a set of 32 different starting points were considered for each configuration to optimize, and a free temporal evolution on 10 ps was performed before quenching. The nudged elastic band (NEB) method was used to find the minimal energy path for the calculation of activation barriers.^{10,24} For the classical TBSMA calculations, we used an unreconstructed gold substrate, consisting of 18 000 Au atoms, distributed on twelve (111) planes, on top of which nanoclusters of various sizes were deposited. NEB calculations were also performed within the density functional theory (DFT) using the projector augmented-wave method²⁵ as implemented in the plane-wave based QUANTUM-ESPRESSO package.²⁶ The exchange-correlation effects were treated using the generalized gradient approximation in the Perdew, Burke, and Ernzerhof form.²⁷ The calculations were performed with a 39 Ry kinetic-energy cutoff and a 909 Ry charge-density cutoff. For the DFT calculations, we used a slab of $8 \times 8 \times 3$ Au atoms plus the cluster of 19 atoms which was extracted from the larger “classical” configuration relaxed by using the TBSMA method. The structural arrangements of the configurations involved in the energy profile were determined by using the classical TBSM approach. We used a $2 \times 2 \times 1$ k -point sampling of the Brillouin zone.

The analysis of the dynamical behavior of the system with temperature was investigated by integrating the differential mean-square displacements of the atoms given by²⁸

$$\frac{d\langle u_\alpha^2 \rangle}{dv} = \frac{h^2}{4\pi m} \frac{n_\alpha(v)}{v} \coth \frac{hv}{2k_B T}, \quad (3)$$

where $n_\alpha(v)$ is the normalized spectral density of vibration along the direction α , m is the mass, T is the temperature, and v is the vibration frequency. The spectral density of vibration was obtained from the temporal Fourier transform of the group average of the momentum autocorrelation function,^{29,30} given by

$$Z_l^{(\alpha)}(t) = \frac{\langle \sum_{i \in l} \int p_i^{(\alpha)}(\tau) p_i^{(\alpha)}(t + \tau) d\tau \rangle}{\langle \sum_{i \in l} \int p_i^{(\alpha)}(\tau) p_i^{(\alpha)}(\tau) d\tau \rangle}. \quad (4)$$

$p_i^{(\alpha)}$ is the α component of the momentum of the atom i , belonging to the group l of atoms (adatoms, surface, and bulk gold atoms).

The momentum autocorrelation function, obtained by approximating the ensemble averages by taking different origins in the time evolution of 32 different initial configurations, is calculated on a time interval of 6 ps, after a minimum equilibrium phase of 10 ps.

III. RESULTS

A. Thermodynamics of the monolayer→bilayer transition

To determine the respective roles of chemical and stress energy contributions, we investigated the growth of three different elements onto the gold surface: (i) Co/Au(111) which is an archetype for demixing tendency, showing a large lattice mismatch, (ii) Pt/Au(111) for demixing tendency and a small lattice mismatch, (iii) Pd/Au(111) for weak mixing tendency and a small lattice mismatch.³¹ As the surface energies of the three elements are comparable and much larger than the gold one,^{31,32} the key element characterizing the differences in the growth modes between Co, Pd and Pt on Au(111) is the interface energy, which contains both chemical and elastic stress contributions.

Figure 1 shows clusters of pure (a) Pt, (b) Pd, and (c) Co for sub-monolayer coverages. Thanks to preferential nucleation, leading to self-organization on Au(111), the cluster size can be easily controlled by the amount of deposited material with very homogeneous size distribution.³³ This holds for many metals, among them Co and Pd. For Pt there is no good self-organization at room temperature, and the lateral size distribution is larger than for Co and Pd, as can be seen in Fig. 1(a). However, the cluster height, which will be the relevant feature in this paper, is also homogeneous as for the two other elements. For Pd and Pt, only clusters of one single atomic layer are observed below a coverage of 0.4 ML [Figs. 1(a) and 1(b)] whereas all clusters are bilayer high for Co [Fig. 1(c)].³⁴⁻⁴¹ For Pt and Pd, above 0.4–0.5 ML, the clusters start to have significant lateral sizes so that nucleation of adatoms from the gas phase becomes possible on top of the monolayer clusters. This can be noted in Fig. 1(b) for Pd, where we can see small parts of a second layer. For Co, there is a transition from monolayer to bilayer first suggested by Tölkes *et al.* from He diffraction measurements.³⁵ Figure 1(d) confirms these measurements and shows the coexistence of monolayer and bilayer clusters. This transition occurs in a very narrow coverage regime, around 0.03 ± 0.01 ML.

On the basis of quenched molecular dynamics calculations, which give the potential energy at 0 K of relaxed clusters, we showed in a previous work that, for cobalt, the monolayer configuration is more stable below about 10 to 20 atoms and that the bilayer configuration is more stable for larger clusters, in agreement with the experiments.^{15,16} However, as we will see, one should not draw definite conclusions. Applying the same type of calculations to Pd and Pt gives similar results. Figure 2 shows the calculated energy difference between the monolayer and bilayer configurations for Co, Pd, and Pt as a function of cluster size. One can notice that in all three cases there is a stability inversion from monolayer to bilayer. We define the critical transition size N_c as the number of atoms where the energies of the two configurations are equal. It varies from approximately 10 to 20 atoms for Co and Pt and to about 30 to 40 atoms for Pd.

Such differences between Co, Pd, and Pt can be understood by considering the role of the surface and interface energies involved in the system. Let us assume two cylindrical clusters containing the same number of atoms, one in a bilayer and the other in a monolayer configuration (see Appendix). In the framework of this model, the critical transition size

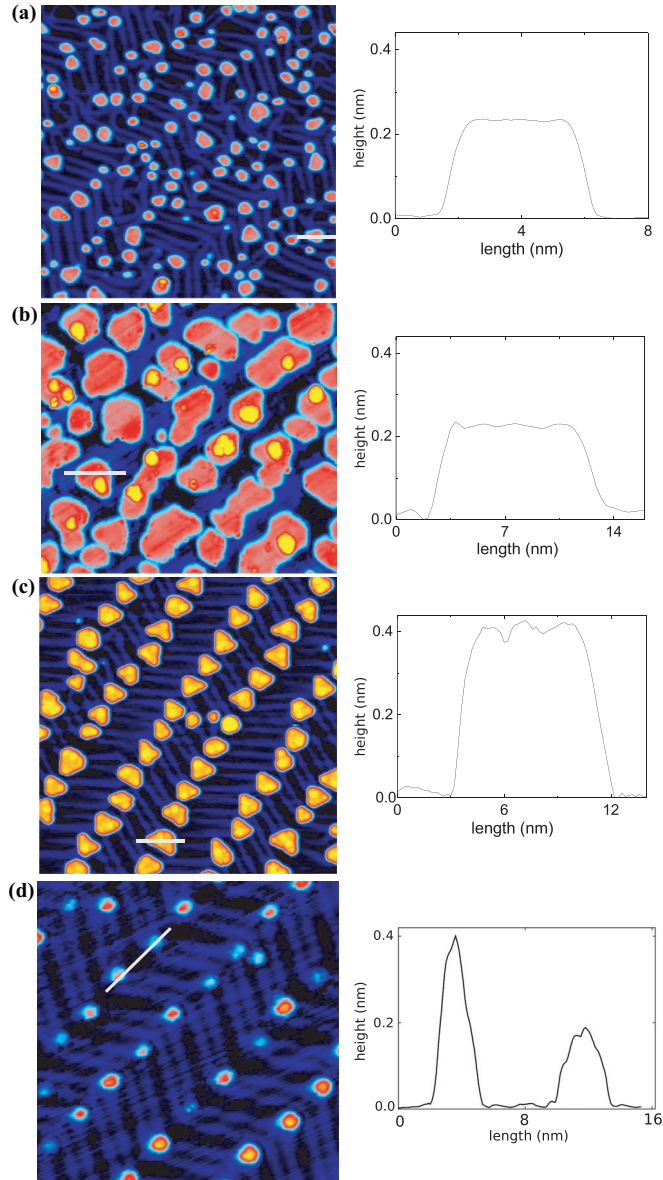


FIG. 1. (Color online) STM images (left) and line profiles (right) on islands marked by white lines for Pt, Pd, and Co deposits on Au(111). (a) 0.1 ML of Pt (80 nm, 1.0 V/0.3 nA). (b) 0.48 ML of Pd (80 nm, 0.6 V/0.5 nA). (c) 0.3 ML of Co (80 nm, 0.6 V/0.4 nA). (d) 0.02 ML of Co (60 nm, 0.3 V/0.1 nA).

reads

$$N_c = 6.64 \frac{\gamma_A'^2}{(\gamma_A + \gamma_I - \gamma_S)^2}, \quad (5)$$

where γ_A , γ_A' , γ_S , and γ_I are respectively the top and lateral surface energies of the adsorbate, the substrate surface energy, and the interface energy. γ_I is the sum of the mixing and elastic energies. Despite a very simple formulation, this model gives a good description of the physics involved in the phenomenon, as demonstrated by the consistence between the critical transition sizes calculated by this model (around 10 for Co and Pt and 30 for Pd) and the ones extracted from the molecular dynamics simulations.

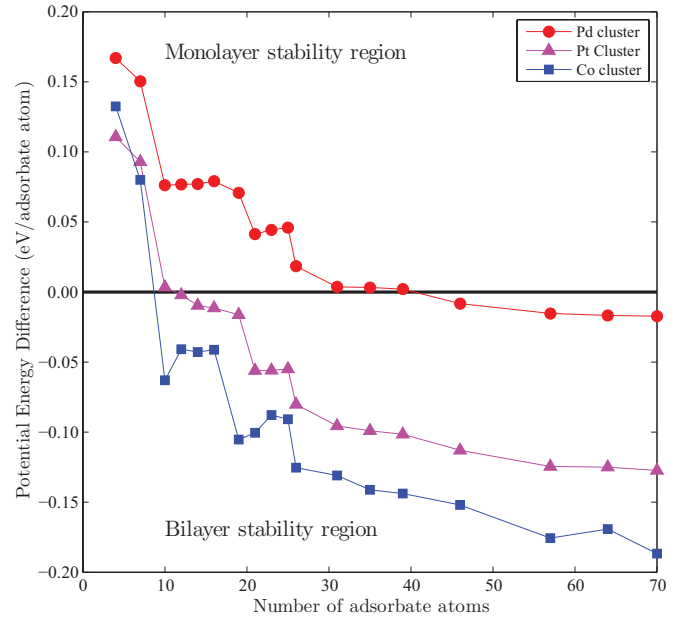


FIG. 2. (Color online) Potential energy difference between the bilayer and monolayer configurations as a function of the number of adsorbate atoms in the cluster.

Equation (5) shows that the bilayer configuration is favored by a large stress at the adsorbate/substrate interface, and by a demixing tendency between adsorbate and substrate. The monolayer to bilayer morphology transition appears thus as a means of (i) partially compensating the surface energy loss ($\gamma_A - \gamma_S$) and (ii) releasing the energy accumulated at the interface between the adsorbate and the substrate during the growth. Note that we use an unreconstructed gold surface, and we therefore neglect possible influence of the surface reconstruction. It was indeed shown that for Co clusters the reconstruction has only a minor influence on the transition.¹⁵ For Pd and Pt, it would allow further stress release, leading to slightly reduced critical transition size. It is, however, clear that this purely thermodynamic approach does not explain the monolayer shape for Pt and Pd clusters, independently of cluster size, since the stability inversion is only observed experimentally for Co.

B. Kinetics of the monolayer \rightarrow bilayer transition

The fact that Pt and Pd clusters do not reach their thermodynamically stable state suggests that mass transport from first plane to the top of the cluster is kinetically hindered. In order to get the origin of this phenomenon and its relationship with the chemical nature of the adsorbate, we use temperature dependent molecular dynamics, which allows us to follow the motion of any atom on a time scale ranging from femtoseconds to nanoseconds.

Clusters of Co, Pd, and Pt of sizes ranging from 8 to 539 atoms were considered, and initially set up in a monolayer configuration. The time evolution is followed for different temperatures ranging from 300 to 600 K.

Figure 3 displays snapshots from the time evolution at 500 K of Co clusters composed of 8, 16, and 30 atoms. For very small cluster sizes [e.g., 8 Co atoms; see Figs. 3(a)–3(d) and

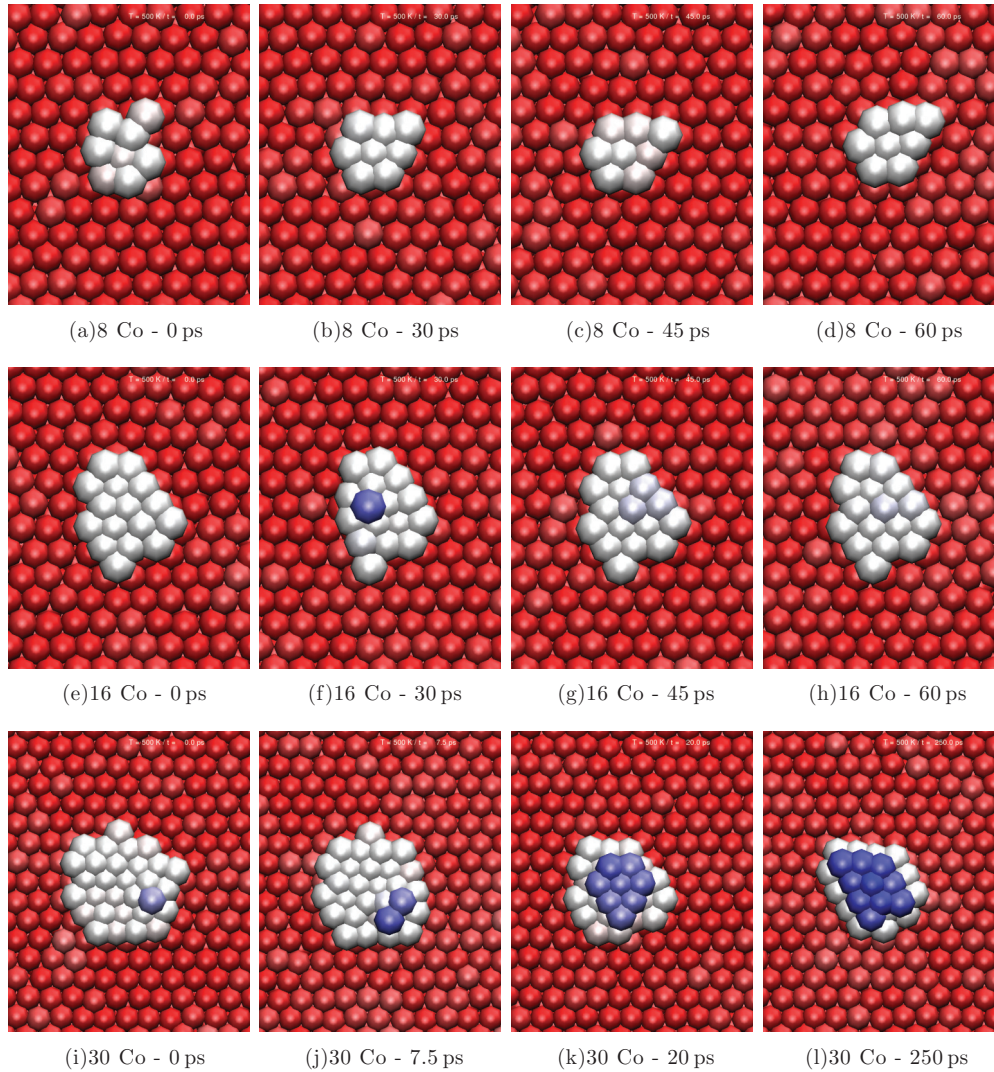


FIG. 3. (Color online) Time evolution of Co clusters at 500 K. Red atoms are gold. The atoms with a color ranging from white to blue (black) are cobalt. The white to blue (black) color range depicts cobalt atoms as a function of height, from first to second plane. (a)–(d) 8 atoms. (e)–(h) 16 atoms. (i)–(l) 30 atoms. See also the videos in the Supplemental Material (Refs. 42–45).

Supplemental Material video Co8.mov],⁴² the Co atoms always remain in the first plane and there is no attempt of movement towards the top of the cluster. For 16 atoms [Figs. 3(e)–3(h) and video Co16.mov],⁴³ fleeting atomic movements towards the second plane, and back, are observed on a time scale of about 2 ps. The cluster, however, mostly stays in a monolayer configuration. From about 20 to 30 Co atoms, the fleeting movements evolve into persistent jumps of atoms towards the second plane [Figs. 3(i)–3(l) and video Co30.mov].⁴⁴ Conversely, for Pd and Pt (see video Pd378.mov)⁴⁵ fleeting movements are never observed, independently of the cluster size. There is no nucleation of a second layer even for clusters as large as 539 atoms, despite of the higher stability of the bilayer configuration (Fig. 2). These calculations are in excellent agreement with the experimental observations. Note that the beginning of a second layer nucleation can be seen above 0.4 ML for Pd (Fig. 1) but, at this coverage, clusters are sufficiently large so that atoms coming from the gas phase can form stable nuclei on the top.

A quantitative description of the transition in the case of a cobalt cluster of 37 atoms is given by Fig. 4 which displays the time evolution of the population of Co atoms in the top plane for various temperatures. At 600 K, the equilibrium shape (bilayer) is reached after 200 ps. At 450 K, 1 ns is needed to reach equilibrium. At 300 K, equilibrium cannot be reached in a reasonable simulation time scale. However, a close look at the Supplemental Material video Co16.mov⁴³ for Co indicates oscillations in the second plane atom population, corresponding to the fleeting movements. For a cluster larger than the critical transition size, the oscillations progressively damp out and transform in persistent jumps (see video Co30.mov).⁴⁴ This suggests that the evolution of atom population is governed by a rate equation whose analytical solution is an exponential growth of type $1 - \exp(-t/\tau)$. τ is a time constant which obeys the Arrhenius equation as shown on Fig. 5. At 300 K one can see that $\tau \approx 20$ ns, meaning that the transition should be completed after $\approx 5\tau$, i.e., about 100 ns.

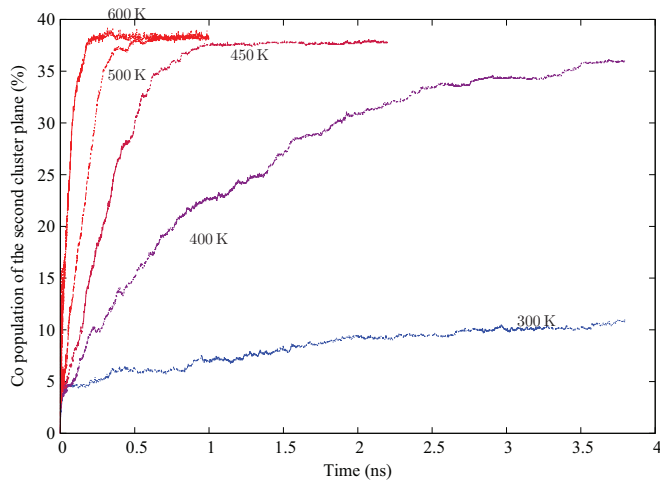


FIG. 4. (Color online) Time evolution for a 37 Co atom cluster of the proportion of atoms in the second cluster plane as a function of temperature.

In order to rationalize the dynamics of the monolayer to bilayer transition, we now investigate the transition from an energy point of view but also from a vibrational aspect. For the transition to occur, the activation energy barriers for moving atoms from the first to second plane must be smaller than thermal energy. Furthermore, the magnitude of atom vibrations must be large enough for inducing movements of the cluster atoms.

C. Energy activation barriers

Calculating the activation energy barriers is not a simple task, since they strongly depend on the pathway followed by an atom in the motion process. The time evolution simulations allow us to determine the most probable pathways and we can therefore give an estimation of the lowest activation energy barriers, following these pathways. Figure 6(a) shows several different initial positions (1–3) of the moving atom and

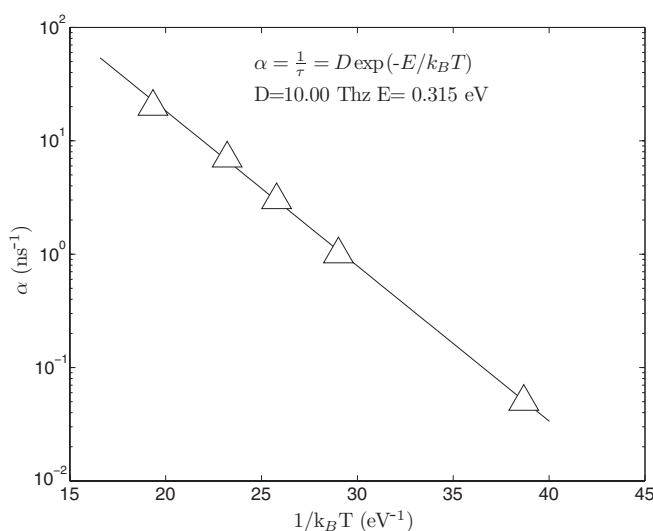


FIG. 5. Evolution of τ with temperature in the case of a 37 Co atom cluster.

TABLE I. Activation barriers (in eV) for moving an atom up from the first cluster plane to the second, as a function of its initial location in the cluster as depicted in Fig. 6, calculated in by using the TBSMA method.

Element	Location		
	(1)	(2)	(3)
Co	1.08	0.80	0.54
Pd	1.31	1.47	1.89
Pt	1.32	1.72	2.00

Table I gives the corresponding energy barriers calculated by the nudged elastic band method.^{10,24} The barriers are indeed much smaller for Co than for Pd and Pt, whatever the pathway considered. The very high barriers for Pd and Pt hinder any motion at the temperatures of interest. One can also notice that the extraction of a Pd or Pt atom from the cluster edge is favored with respect to central atoms, whereas the situation is reversed for Co.

The question is now to understand why the activation energy barrier is so much smaller for Co than for the other two elements. Different contributions may explain such a behavior, including electronic, chemical, and elastic ones. However, the NEB calculations of the energy profile for moving an atom from the first to the second plane show very similar results whatever the method used, either *ab initio* DFT or classical TBSMA. Figure 7 displays energy profiles along the reaction path for moving a Pd atom from the first to the second plane for a Pd cluster of 19 atoms calculated by DFT and classical TBSMA methods. They are very similar and the energy barrier calculated by using the DFT method is only 5% smaller than the one calculated by using classical TBSMA potentials. This evidences the weak influence of the electronic changes due to the atomic rearrangements occurring during the transition on the energy barrier. In addition this comparison provides an indication about the precision of the classical TBSMA approach for the calculation of the energy barrier.

In view of the different characteristics of the three couples of elements, one can say that the dominating contribution is the stress energy. For Pd and Pt the lattice mismatch with the substrate is small, thus the accumulated elastic energy is weak (on the order of 0.2 J/m²; see Appendix) and the relaxed situation is pseudomorphic for both Pd and Pt, leaving the atoms in a stable threefold environment, as evidenced in Figs. 6(c) and 6(d). The energy barrier being mainly dependent on the overall atom-atom binding, it increases from the edge to the center of the cluster (Table I). Conversely, the arrangement of the Co atoms is far from pseudomorphic as can be seen in Figs. 6(a) and 6(b): the large lattice mismatch between Co and Au (14%) would lead to huge accumulation of elastic energy, roughly 2 J/m² (see Appendix). Strong relaxation effects partially release the elastic energy down to 80 mJ/m². This in turn leads to an incommensurate structure which has the effect of putting some Co atoms in twofold-coordinated bridge and on-top positions with respect to the gold substrate.⁴⁶ Consistently with the demixing tendency of the CoAu system, this allows us also to reduce the effective number of unfavorable heteroatomic Co-Au bonds (on the

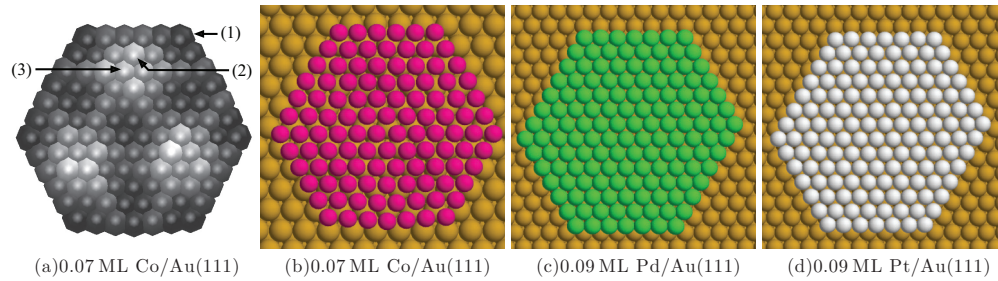


FIG. 6. (Color online) Examples of relaxed monolayer clusters. (a),(b) Co/Au(111). (c) Pd/Au(111). (d) Pt/Au(111). The clusters were relaxed by using a quenched molecular dynamics process giving the equilibrium positions of the atoms at 0 K. The corrugation associated to the Co cluster is given in (a), The white (black) atoms occupy the highest (lowest) positions. The corrugation amplitude is 0.46 Å. The labels (1), (2), and (3) depict the initial positions of the atoms moving up considered for the moving-up activation barrier calculations.

order of 25% for a cluster of 108 atoms). Another consequence is a very high corrugation in the cluster, which can be as large as 0.5 Å in the Co cluster, whereas for Pd and Pt it is always smaller than 0.1 Å. As the cluster size increases, more and more Co atoms get in prejudicial positions with respect to the underlying gold substrate, leading to an increasing corrugation in the cobalt cluster. This corrugation has a crucial role during the growth, facilitating the extraction of Co atoms. An interesting point to note is indeed that the nucleation of the second Co layer occurs close to, but not at the extreme edge of the cluster. The monolayer to bilayer morphology transition of the cluster is a consequence of the release of elastic energy. For Co, the accumulated elastic energy produces important relaxation effects which strongly reduce the energy barriers for atom movements towards the top of the cluster. For Pd and Pt, although the bilayer is thermodynamically favored for larger clusters, the absence of stress release leads to high energy barriers for atom jumping and the clusters therefore stay in a monolayer configuration.

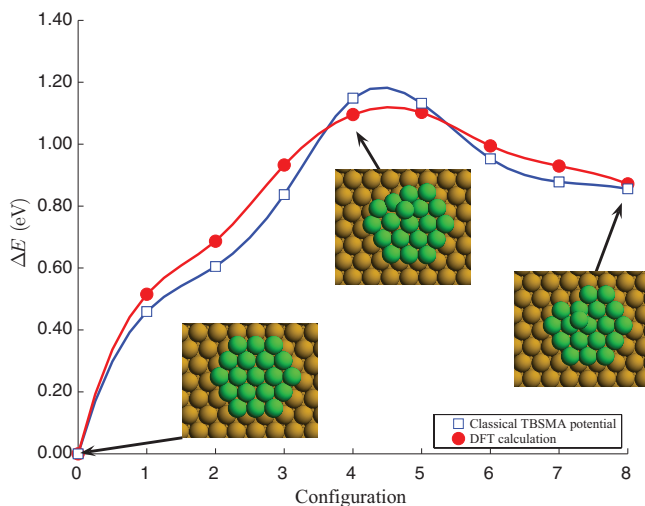


FIG. 7. (Color online) Energy profiles along the reaction path for moving a Pd atom from the first to the second plane calculated in the frameworks of the density functional theory (●) and the TBSMA classical approach (□) for a Pd cluster of 19 atoms. See text for more details.

D. Vibrational considerations

The stress release of the cobalt cluster through relaxation effects has also an important consequence on the magnitude of vibration of the atoms. Figure 8 displays the variations of the mean-square displacements (MSDs) of the adsorbate atoms along the out-of-plane $\langle 111 \rangle$ direction [Fig. 8(a)] and along the in-plane $\langle 110 \rangle$ direction [Fig. 8(b)] as a function of cluster size at $T = 300$ K. We present calculations for Co, Pt, and Pd clusters on Au(111), and for Co on Co(111).

In all cases, nothing special is observed for the out-of-plane MSDs. Conversely, the in-plane MSD for Co/Au(111) is very different from the ones for Pd and Pt. For Pd/Au(111), Pt/Au(111), and also for Co/Co(111) the in-plane MSD is monotonously decreasing with cluster size and becomes rather constant above 15 atoms. On another hand, for Co/Au(111) we observe a strong increase of the in-plane MSD for cluster sizes between 20 and 30 Co atoms, corresponding to the transition range. A direct relationship with the stress inside the cluster is evidenced by comparing the MSD for in-plane Co/Au(111) with Co/Co(111), the corresponding homoepitaxial system. For the latter, the stress inside the Co cluster is small and a monotonous decrease of the MSD, related to the diminution of the low coordinated atom ratio in the cluster, is observed when the cluster grows. The behavior is similar for Pt/Au(111) and Pd/Au(111); these systems can be considered from a stress viewpoint as nearly homoepitaxial.

Equation (3) shows that the MSD is dominated by the low-frequency region of the vibrational density of state. To analyze how the vibrational spectrum is modified by the cluster size, we fix the temperature at $T = 50$ K in order to stay below the transition for Co clusters on Au(111) to avoid morphology changes which would change the vibrational spectrum. Figure 9 displays the differential MSD along the $\langle 110 \rangle$ direction for Co/Au(111) for clusters sizes ranging from 6 to 45 cobalt atoms. For small clusters, one observes peaks at around 0.8 THz which disappear as the clusters grow. These peaks originate from the atoms located at the edge of the clusters. They are at the origin of the large magnitude of vibration at small cluster sizes as observed in Fig. 8.⁴⁷ Despite a large vibrational amplitude, these clusters do not transit because the thermodynamic stable state is monolayer. This explains the fleeting movements observed in the videos. For cluster sizes of 21 and 28 Co atoms additional lower frequency peaks appear at 0.3 THz (Fig. 9). They indicate a softening of

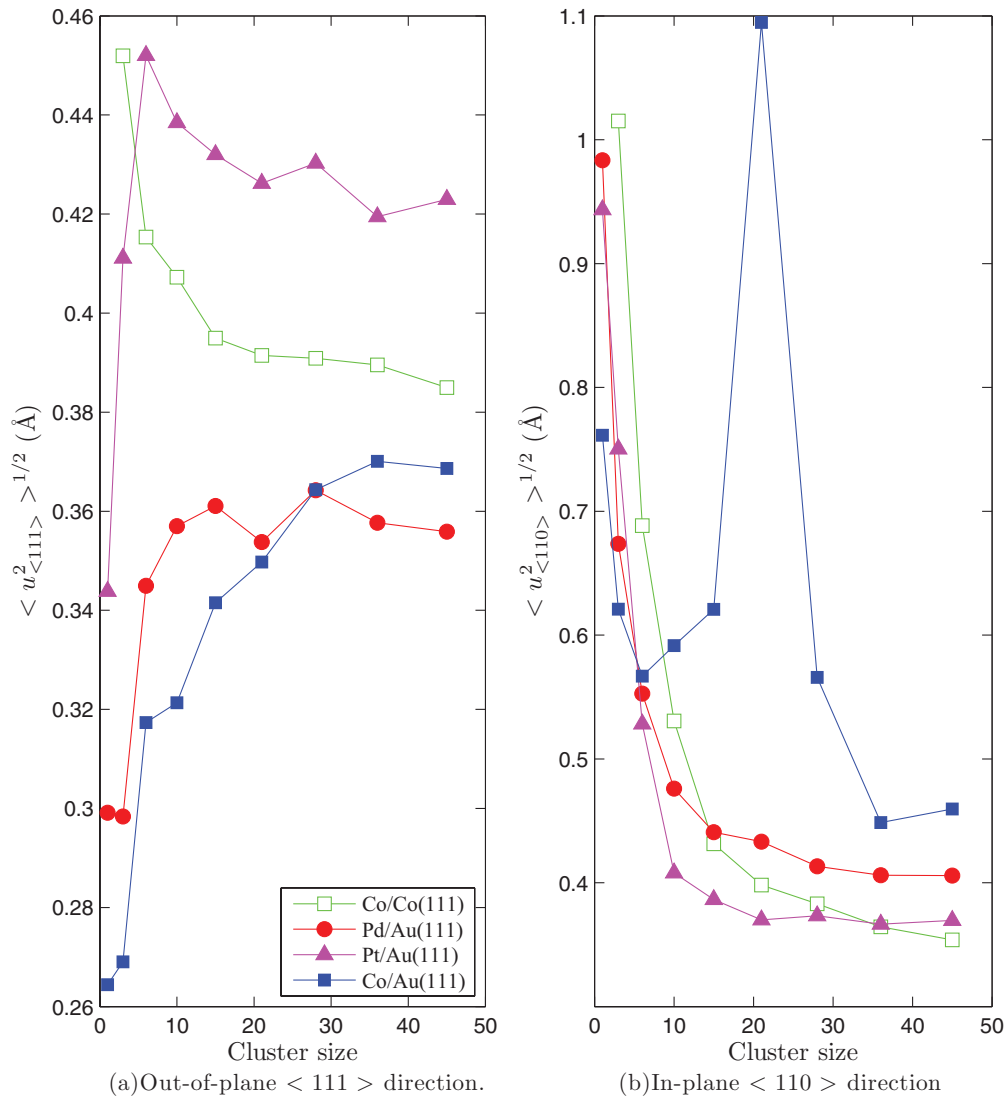


FIG. 8. (Color online) Variation of mean-square displacements of the adsorbate atoms as a function of cluster size at $T = 300$ K along (a) the out-of-plane $\langle 111 \rangle$ direction and (b) the in-plane $\langle 110 \rangle$ direction.

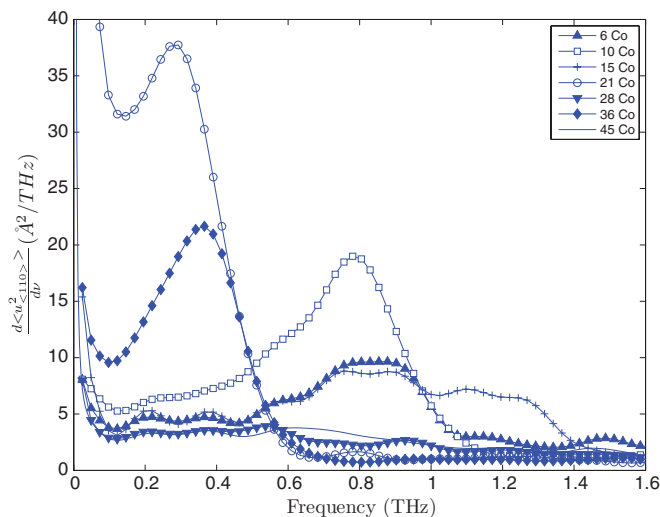


FIG. 9. (Color online) Differential mean-square displacement for Co/Au(111) along the $\langle 110 \rangle$ direction. $T = 50$ K.

the cobalt-cobalt bonds and they are responsible for the very large magnitude of vibration (Fig. 8) in the transition regime.

Due to the large mismatch between cobalt and gold, an increasing dispersion of the interatomic distances between cobalt atoms appears as the cluster grows, as can be drawn from Fig. 10 which displays the standard deviation of the Co-Co first-neighbor distances. It is very similar to an “amorphization” of the cobalt cluster where the excess density of vibrational states at low frequency is due to vibrations of atoms in the strongly anharmonic environment resulting from disorder.^{48–50}

The low-frequency in-plane modes appearing in the 20–30 Co atom clusters grown on Au(111) are fundamental for the mass transport from the first to second plane since they allow the reorganization necessary to induce a global change of cluster shape. Such an in-plane reorganization does not appear for Pd and Pt on Au(111) since the near pseudomorphy of these two elements on gold prevents cluster amorphization and then the appearance of the low frequency in-plane modes.

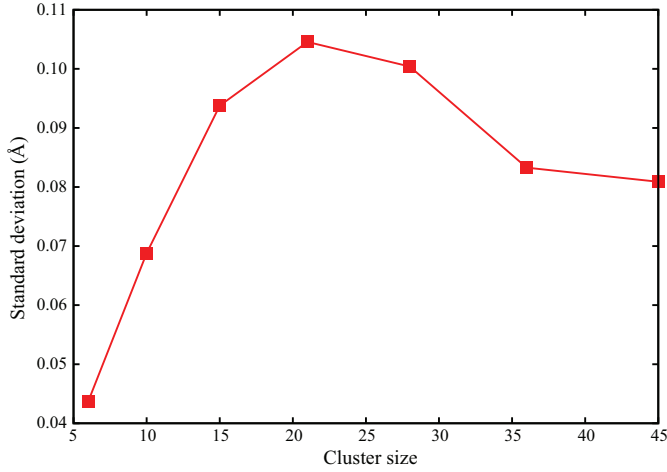


FIG. 10. (Color online) Standard deviation of the Co-Co first-neighbor distances.

IV. CONCLUSION

In summary, atomistic simulations based on realistic potentials reveal the importance of stress release in the morphology of supported clusters, because it governs both thermodynamics and kinetics of cluster formation. Depending on the stress release, morphology transitions towards more stable configurations may occur or not. The simulations give insight about the detailed mechanisms and time scale of the morphology transition and the conditions for this transition to occur. In the case of the equilibrium shape transition of Co clusters on Au(111), the role of stress producing the softening of the vibration modes is highlighted. A potential application of these findings is a better morphology control of cluster shapes. Suitable association of different elements in nanoscale alloy clusters could allow us to operate a fine-tuning of the chemical and elastic energy contributions, thus opening the way for building new materials with selected shapes and properties.

ACKNOWLEDGMENTS

This work has been supported by the Agence Nationale de la Recherche, Program No. ANR-05-NANO-073. We would like to acknowledge J.-G. Faullumel for his technical help in mounting the experimental UHV setup. We are grateful to G. Schull and L. Simon for useful advice. We thank the “Institut du Développement et des Ressources en Informatique Scientifique” (IDRIS) for a grant of computer time (Project No. 090796).

APPENDIX

Let us assume monolayer and bilayer high cylindrical clusters of radius R (r), containing N atoms, h being the height of one monolayer (Fig. 11).

The total energies, referenced to the bare gold slab’s energy, of the monolayer and bilayer configurations are

$$E_m = \pi R^2 \gamma_I - \pi R^2 \gamma_S + \pi R^2 \gamma_A + 2\pi h R \gamma'_A, \quad (\text{A1})$$

$$E_b = \pi r^2 \gamma_I - \pi r^2 \gamma_S + \pi r^2 \gamma_A + 4\pi h r \gamma'_A, \quad (\text{A2})$$

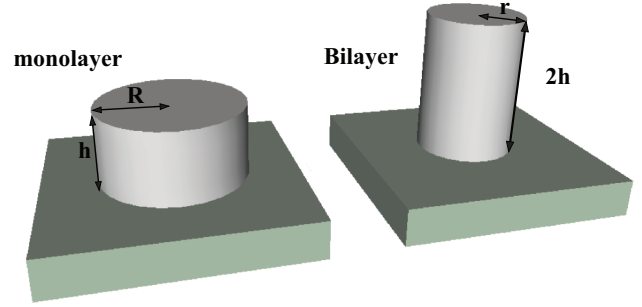


FIG. 11. (Color online) Geometry of the model.

where γ_I and γ_S are respectively the interface and the substrate surface energies per unit area, and γ_A and γ'_A are the on-top and lateral surface energies of the cluster. The on-top surface energy corresponds to the (111) facet whereas the lateral surface energy of the cylinder is taken as the average of the surface energies of the (100), (110), and (111) type facets. The interface energy γ_I is the sum of an elastic contribution γ_{Elas} and mixing energy γ_{Mix} . Ω is the atomic volume of the adsorbate atoms. The radius of the clusters is related to the number of atoms N by

$$h\pi R^2 = 2h\pi r^2 = N\Omega. \quad (\text{A3})$$

The energy difference $\Delta E = E_m - E_b$ between monolayer and bilayer reads

$$\Delta E = \frac{\Omega}{2h} (\gamma_A + \gamma_I - \gamma_S) N - 2(\sqrt{2} - 1) \sqrt{\pi h \Omega} \gamma'_A \sqrt{N}. \quad (\text{A4})$$

The critical transition size from monolayer to bilayer, defined as the cluster size where ΔE vanishes, is then given by

$$N_c = 16\pi(\sqrt{2} - 1)^2 \frac{h^3}{\Omega} \frac{\gamma_A'^2}{(\gamma_A + \gamma_I - \gamma_S)^2}, \quad (\text{A5})$$

and taking $h = \frac{a}{\sqrt{3}}$ and $\Omega = \frac{a^3}{4}$ for a fcc crystal with lattice parameter a , one obtains

$$N_c = 6.64 \frac{\gamma_A'^2}{(\gamma_A + \gamma_I - \gamma_S)^2}. \quad (\text{A6})$$

Tables II–IV give the parameters of the interatomic potentials and elastic coefficients (Tables II and III), and the deduced

TABLE II. Parameters of the interatomic potentials.

Bond	A (eV)	p	ξ (eV)	q	$r^{(0)}$ (Å)
Au-Au	0.189	10.40	1.743	3.87	2.88
Au-Co	0.141	10.63	1.614	3.11	2.69
Au-Pd	0.161	11.24	1.654	3.59	2.82
Au-Pt	0.225	10.77	2.136	3.77	2.83
Co-Co	0.106	10.87	1.600	2.36	2.50
Pd-Pd	0.115	12.07	1.494	3.12	2.75
Pt-Pt	0.242	11.14	2.506	3.68	2.77

TABLE III. Elastic constants of elements used in this paper calculated in the framework of the TBSMA model (Mbar). Calculations performed for face-centered-cubic crystallographic structure. Experimental data are given in parentheses.

	C_{11}	C_{12}	C_{44}	C'	B
Au	1.878(1.87)	1.495(1.54)	0.521(0.45)	0.191(0.17)	1.622(1.65)
Co	2.329	1.624	1.089(1.28)	0.352(0.41)	1.859(1.87)
Pd	2.010(2.32)	1.459(1.78)	0.802(0.73)	0.276(0.26)	1.642(1.96)
Pt	3.230(3.41)	2.493(2.73)	1.032(0.91)	0.368(0.34)	2.739(2.96)

energies (Table IV). The mixing energies are given by the difference between the enthalpy of the mixed elements (X and Au with $X = \text{Co, Pd, or Pt}$) and the sum of the enthalpies of the separated components at the same pressure and temperature. The enthalpies are taken from Ref. 31. The surface energies, γ_A and γ'_A , and the elastic energy term γ_{Elas} are calculated in the framework of the second-moment approximation of the tight

TABLE IV. Calculated surface and elastic energies, and mixing energies. Note that only the difference in surface energies is preserved but not the absolute values (Ref. 18).

Element	γ_A (J/m ²)	γ'_A (J/m ²)	γ_{Elas} (J/m ²)	γ_{Mix} (J/m ²)
Co	1.47	1.90	0.08	0.66
Pt	1.12	1.46	0.23	0.43
Pd	0.94	1.24	0.21	0.00
Au	0.56			

binding theory.¹⁷ For the elastic energy contribution, a uniform in-plane strain is considered, leading to the expression

$$\gamma_{\text{Elas}} = \frac{2}{3} \frac{a}{\Omega} \eta^2 (C_{11} + 2C_{12} + C_{44}), \quad (\text{A7})$$

where $\eta = \frac{a_s - a}{a}$ is the mismatch between the adsorbate and the substrate, and a and a_s are respectively the lattice parameters of the adsorbate and substrate.

*herve.bulou@ipcms.u-strasbg.fr

- ¹M. Faraday, *Philos. Trans. R. Soc. London* **147**, 145 (1857).
²J. L. Carter, J. A. Cusumano, and J. H. Sinfelt, *J. Phys. Chem.* **70**, 2257 (1996).
³W. A. de Heer, P. Milani, and A. Châtelain, *Phys. Rev. Lett.* **65**, 488 (1990).
⁴W. A. de Heer, K. Selby, V. Kresin, J. Masui, M. Vollmer, A. Châtelain, and W. D. Knight, *Phys. Rev. Lett.* **59**, 1805 (1987).
⁵I. O. Sosa, C. Noguez, and R. G. Barrera, *J. Phys. Chem. B* **107**, 6269 (2003).
⁶A. Miyazaki, I. Balint, and Y. Nakano, *J. Nanopart. Res.* **5**, 69 (2003).
⁷M. Sorescu, R. A. Brand, D. Mihaila-Tarabasanu, and L. Diamandescu, *J. Appl. Phys.* **85**, 5546 (1999).
⁸H. Bulou and C. Massobrio, *J. Phys. Chem. C* **112**, 8743 (2008).
⁹K. L. Man, M. C. Tringides, M. M. T. Loy, and M. S. Altman, *Phys. Rev. Lett.* **101**, 226102 (2008).
¹⁰H. Bulou and C. Massobrio, *Phys. Rev. B* **72**, 205427 (2005).
¹¹H. Bulou and J.-P. Bucher, *Phys. Rev. Lett.* **96**, 076102 (2006).
¹²L. Huang, C. Z. Wang, M. Z. Li, and K. M. Ho, *Phys. Rev. Lett.* **108**, 026101 (2012).
¹³J. B. Hannon, J. Tersoff, and R. M. Tromp, *Science* **295**, 299 (2002).
¹⁴C. R. Henry, *Prog. Surf. Sci.* **80**, 92 (2005).
¹⁵I. Chado, C. Goyhenex, H. Bulou, and J. P. Bucher, *Phys. Rev. B* **69**, 085413 (2004).
¹⁶I. Chado, C. Goyhenex, H. Bulou, and J.-P. Bucher, *Appl. Surf. Sci.* **226**, 178 (2004).
¹⁷V. Rosato, M. Guillopé, and B. Legrand, *Phil. Mag. A* **59**, 321 (1989).
¹⁸C. Goyhenex, *Surf. Sci.* **606**, 325 (2012).
¹⁹C. Goyhenex and H. Bulou, *Phys. Rev. B* **63**, 235404 (2001).
²⁰L. Verlet, *Phys. Rev.* **159**, 98 (1967).
²¹W. C. Swope, H. C. Andersen, P. H. Berens, and K. R. Wilson, *J. Chem. Phys.* **76**, 637 (1982).

- ²²B. Legrand, G. Tréglia, M. C. Desjonquères, and D. Spanjaard, *J. Phys. C* **19**, 4463 (1986).
²³E. Bitzek, P. Koskinen, F. Gähler, M. Moseler, and P. Gumbsch, *Phys. Rev. Lett.* **97**, 170201 (2006).
²⁴G. Henkelman and H. Jónsson, *J. Chem. Phys.* **113**, 9978 (2000).
²⁵P. E. Blöchl, *Phys. Rev. B* **50**, 17953 (1994).
²⁶QUANTUM-ESPRESSO is a community project for high-quality quantum-simulation software, based on density-functional theory, and coordinated by Paolo Giannozzi. See <http://www.quantum-espresso.org> and <http://www.pwscf.org>.
²⁷J. P. Perdew, K. Burke, and M. Ernzerhof, *Phys. Rev. Lett.* **77**, 3865 (1996).
²⁸M. C. Desjonquères and D. Spanjaard, *Concepts in Surface Physics* (Springer, Berlin, 1996).
²⁹J. M. Dickey and A. Paskin, *Phys. Rev.* **188**, 1407 (1969).
³⁰P. D. Ditlevsen, P. Stoltze, and J. K. Nørskov, *Phys. Rev. B* **44**, 13002 (1991).
³¹F. R. de Boer, R. Boom, W. C. M. Mattens, A. R. Miedema, and A. K. Niessen, *Cohesion in Metals*, Vol. 1 (North Holland, Amsterdam, 1998).
³²W. R. Tyson and W. A. Miller, *Surf. Sci.* **62**, 267 (1977).
³³H. Brune, *Surf. Sci. Rep.* **31**, 125 (1998).
³⁴B. Voigtländer, G. Meyer, and N. M. Amer, *Phys. Rev. B* **44**, 10354 (1991).
³⁵Ch. Tölkes, P. Zeppenfeld, M. A. Krzyzowski, R. David, and G. Comsa, *Phys. Rev. B* **55**, 13932 (1997).
³⁶C. J. Baddeley, C. J. Barnes, A. Wander, R. M. Ormerod, D. A. King, and R. M. Lambert, *Surf. Sci.* **314**, 1 (1994).
³⁷C. J. Baddeley, R. M. Ormerod, A. W. Stephenson, and R. M. Lambert, *J. Phys. Chem.* **99**, 5146 (1995).
³⁸A. W. Stephenson, C. J. Baddeley, M. S. Tikhov, and R. M. Lambert, *Surf. Sci.* **398**, 172 (1998).
³⁹T. Suzuki, Y. Hasegawa, Z.-Q. Li, K. Ohno, Y. Kawazoe, and T. Sakurai, *Phys. Rev. B* **64**, 081403 (2001).
⁴⁰C. S. Casari, S. Foglio, F. Siviero, A. Li Bassi, M. Passoni, and C. E. Bottani, *Phys. Rev. B* **79**, 195402 (2009).

- ⁴¹Y. Nahas, V. Repain, C. Chacon, Y. Girard, and S. Rousset, *Surf. Sci.* **604**, 829 (2010).
- ⁴²See Supplemental Material at <http://link.aps.org/supplemental/10.1103/PhysRevB.87.155404> for video Co8.mov.
- ⁴³See Supplemental Material at <http://link.aps.org/supplemental/10.1103/PhysRevB.87.155404> for video Co16.mov.
- ⁴⁴See Supplemental Material at <http://link.aps.org/supplemental/10.1103/PhysRevB.87.155404> for video Co30.mov.
- ⁴⁵See Supplemental Material at <http://link.aps.org/supplemental/10.1103/PhysRevB.87.155404> for video Pd378.mov.
- ⁴⁶Early stress release in ultrathin films was indeed evidenced by H. Arduin, E. Snoek, and M.-J. Casanove, *J. Cryst. Growth* **182**, 394 (1997).
- ⁴⁷A. Kara and T. S. Rahman, *Phys. Rev. Lett.* **81**, 1453 (1998).
- ⁴⁸N. Lustig, J. S. Lannin, J. M. Carpenter, and R. Hasegawa, *Phys. Rev. B* **32**, 2778 (1985).
- ⁴⁹N. Lustig, J. S. Lannin, and R. Hasegawa, *Phys. Rev. B* **34**, 6725 (1986).
- ⁵⁰V. K. Malinovsky, V. N. Novikov, P. P. Parshin, A. P. Sokolov, and M. G. Zemlyanov, *Europhys. Lett.* **11**, 43 (1990).